ORIGIN OF SPATIAL VARIATIONS OF SCATTERING POLARIZATION IN THE WINGS OF THE Ca I 4227 Å line

M. Sampoorna[1], J. O. Stenflo[2], K. N. Nagendra[1], M. Bianda[2,3], R. Ramelli[3], and L. S. Anusha[1]
[1] Indian Institute of Astrophysics, Koramangala, Bangalore 560 034, India
[2] Institute of Astronomy, ETH Zürich, CH-8093 Zürich, Switzerland
[3] Istituto Ricerche Solari Locarno, Via Patocchi, CH-6605 Locarno-Monti, Switzerland

ABSTRACT

Polarization that is produced by coherent scattering can be modified by magnetic fields via the Hanle effect. This has opened a window to explorations of solar magnetism in parameter domains not accessible to the Zeeman effect. According to standard theory the Hanle effect should only be operating in the Doppler core of spectral lines but not in the wings. In contrast, our observations of the scattering polarization in the Ca I 4227 Å line reveal the existence of spatial variations of the scattering polarization throughout the far line wings. This raises the question whether the observed spatial variations in wing polarization have a magnetic or nonmagnetic origin. A magnetic origin may be possible if elastic collisions are able to cause sufficient frequency redistribution to make the Hanle effect effective in the wings without causing excessive collisional depolarization, as suggested by recent theories for partial frequency redistribution (PRD) with coherent scattering in magnetic fields. To model the wing polarization we bypass the problem of solving the full polarized radiative transfer equations and instead apply an extended version of the technique based on the "last scattering approximation." It assumes that the polarization of the emergent radiation is determined by the anisotropy of the incident radiation field at the last scattering event. We determine this anisotropy from the observed limb darkening as a function of wavelength throughout the spectral line. The empirical anisotropy profile is used together with the single-scattering redistribution matrix, which contains all the PRD, collisional, and magnetic field effects. The model further contains a continuum opacity parameter, which increasingly dilutes the polarized line photons as we move away from the line center, and a continuum polarization parameter that represents the observed polarization level far from the line. This model is highly successful in reproducing the observed Stokes Q/I polarization (linear polarization parallel to the nearest solar limb), including the location of the wing polarization maxima and the minima around the Doppler core, but it fails to reproduce the observed spatial variations of the wing polarization in terms of magnetic field effects with frequency redistribution. This null result points in the direction of a nonmagnetic origin in terms of local inhomogeneities (varying collisional depolarization, radiation-field anisotropies, and deviations from a plane-parallel atmospheric stratification).

Key words: line: formation – magnetic fields – polarization – scattering – Sun: atmosphere

1. INTRODUCTION

Coherent scattering on the Sun produces a linearly polarized spectrum that is as rich in spectral structures as the ordinary intensity spectrum, but has an entirely different appearance since the underlying physical processes are different (see Stenflo 2004a). This linearly polarized spectrum, which goes under the name the "Second Solar Spectrum," is modified by magnetic fields via the Hanle effect. It allows aspects of solar magnetism to be explored which are not accessible by the Zeeman effect, in particular the vast amounts of "hidden" magnetic fields that have been revealed by Hanle-effect observations (Trujillo Bueno et al. 2004; see also Stenflo 2004b).

The atlas of the Second Solar Spectrum (Gandorfer 2000, 2002, 2005) provides an overview of the linear polarization in lines observed near the solar limb, from the UV at 3160 Å to the red at 6995 Å. The largest degree of linear polarization in the visible spectrum is exhibited by the Ca I 4227 Å line. Spatial variations of the linear polarization in the line core due to the Hanle effect have been observed in regions with variable magnetic fields. Spectropolarimetric measurements in this line can be used to explore the magnetic field in the mid-chromosphere (Bianda et al. 1998a, 1998b).

Recent observations by Bianda et al. (2003) in the Ca I 4227 Å line have revealed enigmatic behavior of the line wing polarization. These observations were made in active regions with the spectrograph slit perpendicular to the solar limb.

They showed for the first time spatial variations of the linear polarization (Q/I and U/I) in the far wings of the line, in contradiction with theoretical expectations. We will refer to this unexpected phenomenon as the "(Q/I, U/I) wing signatures." This observation contradicts the long-held standard theory for the Hanle effect, according to which the Hanle effect should only be effective in the line core but not in the line wings. The polarization is expected to approach the nonmagnetic Rayleigh scattering limit in the line wings (see Omont et al. 1973; Stenflo 1994; Landi Degl'Innocenti & Landolfi 2004 for details). In the present paper, we report further such observations, this time done in quiet regions with the slit placed parallel to the nearest solar limb. Again we find similar spatial variations in the line wings as seen before in active regions.

Bianda et al. (2003) suggested a qualitative explanation for the observed (Q/I, U/I) wing signatures in terms of partial frequency redistribution (PRD) and radiative transfer (multiple scattering) effects in the wings of strong resonance lines. Thus, in a balanced mixture of coherent and noncoherent scattering, it is possible to generate Hanle depolarization in the wings as follows: Hanle precession of the oscillating dipole moment is first generated near the resonance (in the line core), but gets shifted to a wing frequency by an elastic collision without destroying the atomic polarization. The atom subsequently emits the photon at the shifted frequency in the line wing. This process would be the source of the (Q/I, U/I) wing signatures. Multiple scattering in the medium (due to finite monochromatic optical

depth in the wings of strong resonance lines) may enhance this effect. Nagendra et al. (2002, 2003) showed through radiative transfer calculations that angle-dependent (AD) PRD is more efficient in generating shallow (Q/I, U/I) wing peaks by this mechanism than the angle-averaged (AA) PRD.

In the present paper, we explore the above suggestions, using the last scattering approximation (LSA) instead of full radiative transfer modeling, which is sufficient for our purpose of verifying the validity of the Hanle wing effect as an explanation of the observed wing polarization variations. This leads us to the rather unexpected conclusion that the Hanle effect cannot explain the observed wing effects, which suggests that the spatial variations of the wing polarization have a nonmagnetic origin. For the scattering theory we use the recently developed Hanle–Zeeman AD PRD matrices for arbitrary magnetic fields (Sampoorna et al. 2007a, 2007b; see also Sampoorna et al. 2009).

In Section 2, we present the observations of the (Q/I, U/I) wing signatures. Section 3 describes our theoretical model. The model fitting to the observed data is discussed in Section 4, while the conclusions are presented in Section 5.

2. OBSERVATIONS OF THE (Q/I, U/I) WING SIGNATURES

2.1. Data Acquisition

Spectropolarimetric recordings of the full Stokes vector were obtained for the Ca I 4227 Å line with the 45 cm aperture Gregory Coudé Telescope (GCT) at IRSOL (Locarno, Switzerland). The ZIMPOL-2 polarimeter system was used (Gandorfer et al. 2004), allowing highly precise measurements that are free from seeing-induced spurious effects, with an accuracy only limited by photon statistics. The observations were performed during the years 2005–2007 over 27 days. In total 86 positions at different limb distances and at various latitudes on the solar disk were recorded, with the spectrograph slit parallel to the limb (which defines the positive Stokes Q direction). Dark frames as well as flat fields were recorded before and/or after the observations. The polarimetric calibration and data reduction procedure have been described in Gandorfer et al. (2004).

The instrumental polarization in the GCT is mainly a function of declination and can be considered constant during a full observing day. Cross-talk from Stokes I to the other Stokes parameters is determined from flat field measurements in quiet regions at disk center. Since in the present analysis we are interested in the linear polarization away from active regions, we selected only regions where Zeeman-like signatures in the Stokes V/I images are sufficiently small, so that the circular-to-linear polarization cross-talk is negligible. We note that the circular-to-linear cross-talk reaches its maximum at the solstices and is always smaller than 25% (Ramelli et al. 2005).

It was carefully checked that the observed small signatures in the linear polarization were not of instrumental origin. To make sure that the observed signatures in the line wings do not originate from differential efficiencies of the different pixel rows of the ZIMPOL CCD, we alternated measurements by shifting the telescope image back and forth by 10″ along the spectrograph slit direction. This could be achieved with the help of the automatic guiding system (Küveler et al. 2003).

2.2. Observational Results

Spatially varying linear polarization structures in the wings (of Stokes Q and/or U) are found in 46 observations out of 86, thus in approximately half of all our recordings. This frequency
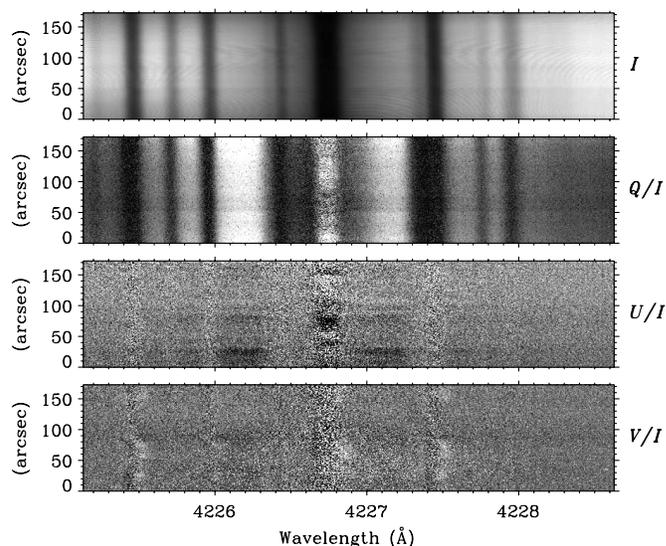

Figure 1. CCD images of the Stokes parameters recorded with the spectrograph slit parallel to the limb (5″ inside the limb). Note the depolarization signatures in the Q/I wings in the 55″–75″ spatial interval. Corresponding U/I wing signatures are seen at the same wavelength positions, but at a different spatial location, for example, in the 20″–30″ interval.

of occurrence represents a *lower* limit, since nonoptimum seeing conditions may smear the features to make them disappear below the noise level. Our observations thus show that such wing signatures (in Q/I and/or U/I) are a very common phenomenon that is likely to be seen in the great majority of cases if the recordings are made with high spatial resolution. We illustrate in Figure 1 a representative example of an observation obtained on 2007 October 5 near the heliographic north pole at about 5″ inside the limb. The spectrograph slit width was 125 μm, which corresponds to 1″, and its length corresponded to about 170″. The total exposure time was 225 s. A second measurement (not shown) taken with the slit shifted by 10″ along the limb (and the slit) direction confirmed that the signatures were related to the solar positions and not to the position on the CCD.

The intensity image shows the broad Ca I line at 4226.74 Å with blend lines in the wings. Due to the limb curvature, the largest limb distance from the slit position is reached at around 85″ from the image bottom, while at 0″ and 170″ the distance from the limb is minimum. This explains the brightness variation in the intensity image along the spatial direction.

The strong polarization signatures seen in Q/I are due to scattering polarization. They occur both in the line core and wings, but decrease in amplitude in the very far wings. At the locations of the blend lines in the intensity image we also see the depolarization effects caused by these lines in the Q/I image (Fluri & Stenflo 2001). In the line core we see spatial variations (along the slit) both in Q/I and U/I, which are caused by the Hanle effect (Bianda et al. 1998a, 1998b, 1999) in the presence of magnetic fields in the mid-chromosphere. The Q/I polarization in the Ca I 4227 Å line wings increases at the edges of the spectrograph slit, since the edges are located closer to the solar limb. Narrow horizontal strips that can be seen, for instance, in the interval 55″–75″ from the bottom of the Q/I image show enigmatic "depolarization signatures" in the line wings which we want to explore.

The U/I image shows features in the line core that are due to the Hanle rotation of the polarization plane. However, structures
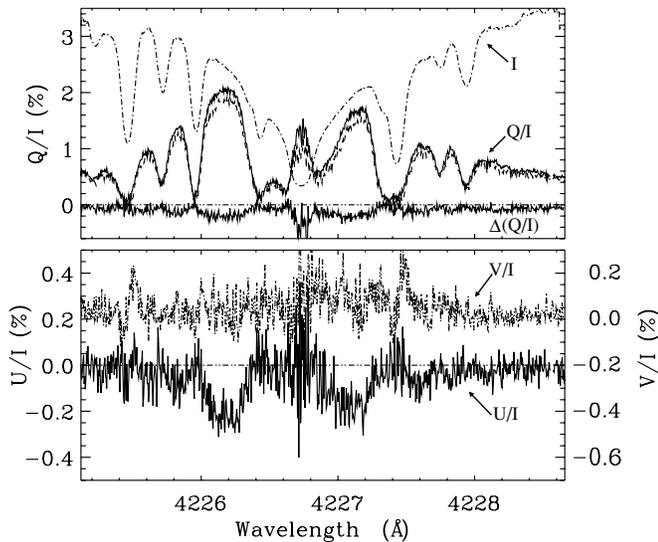
Figure 2. Stokes I, Q/I, U/I, V/I profiles extracted from Figure 1. The heliocentric angle corresponds to $\mu = 0.1$. Note the depolarization in the Q/I wings and the U/I signatures at the corresponding wavelength positions. In the present paper, we refer to them together as the "$(Q/I, U/I)$ wing signatures."

can also be observed in the line wings but at different spatial locations than the line core features, i.e., in the intervals 20″–30″, 40″–50″, and 70″–80″. We note that there are hardly any spatial correlations between the Q/I and U/I wing signatures.

Figure 2 shows profiles averaged over different spatial intervals. In the top panel, the dot-dashed line represents the intensity profile, in arbitrary units, averaged over a 40″ broad interval around the middle of the spectrograph slit. The Q/I profile shown by the solid line is obtained by averaging outside the interval where depolarization in the line wings is observed, while the dashed line represents the profile obtained by averaging in the interval between 55″ and 75″. The difference between the two averaged Q/I profiles is shown by the $\Delta(Q/I)$ line.

In the bottom panel of Figure 2, the solid line represents the U/I profile averaged over the spatial interval 29″–40″. Its shape resembles a negative version of the Q/I profile. Note that the Stokes U/I wing signals of Figures 1 and 2 cannot be due to the possibility that the positive Stokes Q direction may not be exactly parallel to the nearest limb, because in that case the wing polarization in U/I would simply be proportional to the wing polarization in Q/I all along the slit, which is not the case. It is important to note that in our observations the Q/I and U/I wing polarizations never vary in synchrony along the slit but have different spatial structures.

The V/I profile represented by the dotted line is averaged in the interval where the largest polarization amplitudes are seen (24″–45″). Only very faint signatures can be seen in the Fe I lines at 4225.46 and 4227.44 Å. The absence of large signals in V/I shows that we are observing a solar region with very weak longitudinal magnetic field components.

3. THEORETICAL MODEL

Quantitative modeling of the scattering polarization with the Hanle effect requires the solution of the relevant radiative transfer problem. Such calculations have been done by Faurobert-Scholl (1992), Faurobert et al. (2009 and references cited therein), and Holzreuter et al. (2005, 2006), who use AA PRD. Extensive radiative transfer calculations have also been done by Trujillo Bueno and co-workers (see Trujillo Bueno 2009

and references cited therein) to model the scattering line polarization and the Hanle effect in terms of the complete frequency redistribution (CRD) approximation, but taking into account atomic level polarization in multilevel atomic systems.

For exploratory purposes we can avoid such full-scale radiative transfer modeling by using semi-empirical approaches in terms of the LSA, which has proven successful in the past (Stenflo 1982). In the present section, we describe how LSA in combination with the full redistribution matrix for arbitrary magnetic fields can be used to model the Second Solar Spectrum. We illustrate this approach by applying it to the Ca I 4227 Å line observations presented in Section 2.

One of the earliest works on modeling the linearly polarized solar spectrum with LSA dates back to Stenflo (1980), where the observed Ca II H and K line wing polarization that exhibited a quantum interference signature extending over about 200 Å was fitted. In a later paper, Stenflo (1982) extended the LSA concept to interpret Hanle polarization observations of several spectral lines in terms of a micro-turbulent magnetic field, which allowed the strength of the "hidden" tangled fields to be estimated for the first time.

In the present paper, we extend this approach to the exploration of the Hanle effect for partially resolved magnetic fields, which produce signatures in both Q/I and U/I. In the following subsections, we revisit each of the important ingredients of Stenflo's method, for the purpose of clarity and completeness.

3.1. Last Scattering Approximation

The concept of LSA is particularly useful in astronomical contexts where either (1) the geometry is too complicated or (2) the relevant transfer equation is difficult to solve computationally. Recent applications of this concept in the modeling of scattering polarization can be found in Faurobert & Arnaud (2002; modeling of molecular emission lines), Stenflo (2005; modeling the solar continuum polarization), Belluzzi et al. (2007; modeling of the Ba II D$_2$ line), and Frisch et al. (2009; Hanle scattering in random magnetic fields—where a variant of the LSA idea is presented).

LSA exploits the fact that the polarization of the radiation that escapes the atmosphere is mainly determined by the anisotropy of the radiation field at the place where the last scattering process takes place. Since the polarization amplitudes in the lines are small, the polarization of the incident radiation at the last scattering event can be neglected. In other words, the emergent polarization is produced in a single scattering event (the very last one) rather than through multiple scattering within the atmosphere.

In the practical application of this idea the most important limiting assumption is that we base the radiation field anisotropy that we apply to the single-scattering event on the observed limb darkening function which represents the top of the atmosphere. In reality most of the observed photons originate from $\tau \approx \mu$. This difference, however, becomes negligible for extreme limb observations ($\mu \rightarrow 0$), for which the emergent radiation represents the topmost layers of the atmosphere ($\tau \approx 0$). If frequency coherent scattering in the laboratory frame is assumed, LSA allows us to write the emergent Q/I polarization for nonmagnetic scattering in a neatly factorized form

$$\frac{Q}{I} \equiv P = W_{2,\text{eff}}\, k_{\text{G},\lambda}(\mu)\, k_c, \tag{1}$$

where $\mu = \cos\theta$, with θ being the heliocentric angle (see Stenflo 1994). Here, $W_{2,\text{eff}}$ is the effective atomic polarizability factor,

which is unity for the Ca ı 4227 Å line, since it behaves like classical dipole scattering. The blend lines, on the other hand, generally do not polarize, which means that they have a $W_2 = 0$. Their nonpolarizing opacity therefore dilutes the polarized Ca ı 4227 Å line photons, making the "effective polarizability" $W_{2,\text{eff}}$ much smaller than unity inside the blend lines. $k_{G,\lambda}(\mu)$ is a geometric depolarization factor that depends on the anisotropy of the radiation field and the line of sight with respect to the local normal. It describes the depolarization caused by the angular integration over the incident radiation. In practice, this factor is determined from the observed center-to-limb variation (CLV) of Stokes I (see Section 3.2). k_c is the collisional depolarization factor given by $\Gamma_R/(\Gamma_R + \Gamma_E)$, where Γ_R and Γ_E are radiative and elastic collision rates.

3.2. Empirical Determination of the Anisotropy Factor $k_{G,\lambda}(\mu)$

$k_{G,\lambda}(\mu)$ can be determined using the observed limb darkening function, which is defined as follows:

$$c_\lambda(\mu) \equiv \frac{I_\lambda(\mu)}{I_\lambda(\mu = 1)}. \qquad (2)$$

However, what is actually observed is a series of unnormalized spectra $b(\mu)I_\lambda(\mu)$, where $b(\mu)$ is some arbitrary scaling factor that is different for each μ. To eliminate the arbitrary $b(\mu)$ we normalize each spectrum to the continuum intensity. Since a true continuum is usually not recorded, we choose a reference wavelength λ_{ref} at which we are as close to the continuum as we can be. Further, we assume that the CLV at that reference wavelength is the same as the CLV of the continuum, namely

$$\frac{I_{\lambda_{\text{ref}}}(\mu)}{I_{\lambda_{\text{ref}}}(\mu = 1)} \approx \frac{I_c(\mu)}{I_c(\mu = 1)}. \qquad (3)$$

The observed quantity that we have to work with is

$$I_{\text{obs},\lambda}(\mu) = \frac{b(\mu) \, I_\lambda(\mu)}{b(\mu) \, I_{\lambda_{\text{ref}}}(\mu)}, \qquad (4)$$

for each spectrum, so that $b(\mu)$ divides out. We can then write the limb darkening function as

$$c_\lambda(\mu) = \frac{I_{\text{obs},\lambda}(\mu)}{I_{\text{obs},\lambda}(\mu = 1)} \, \frac{I_c(\mu)}{I_c(\mu = 1)}. \qquad (5)$$

For the limb darkening function of the continuum around the 4227 Å line we use the following analytical representation:

$$\frac{I_c(\mu)}{I_c(\mu = 1)} = 1 - a_{0,c} - a_{1,c} + a_{0,c} \, \mu + a_{1,c} \, \mu^2, \qquad (6)$$

where $a_{0,c}$ and $a_{1,c}$ are fit parameters taken from Pierce (2000). The limb darkening function $c_\lambda(\mu)$ determined from the observed data is then fitted by the following function:

$$f_\lambda(\mu) = 1 - a_{0,\lambda} - a_{1,\lambda} + a_{0,\lambda} \, \mu + a_{1,\lambda} \, \mu^2. \qquad (7)$$

Least-squares fitting of $c_\lambda(\mu)$ in terms of $f_\lambda(\mu)$ gives us the values of the coefficients $a_{0,\lambda}$ and $a_{1,\lambda}$. It is important to note that the λ_{ref} chosen should be kept the same for all the recordings of Stokes I with different μ values.

For use with LSA we obtain the geometric depolarization factor $k_{G,\lambda}(\mu)$ by multiplying the Rayleigh phase matrix with

an unpolarized Stokes vector $(I, \, 0, \, 0, \, 0)^T$ and integrating over all the incoming angles. This gives (see Stenflo 1982, 2005)

$$k_{G,\lambda}(\mu) = G_\lambda(1 - \mu^2)/I_\lambda(\mu), \qquad (8)$$

where

$$G_\lambda = \frac{3}{16} \int_{-1}^{+1} (3\mu'^2 - 1) I_\lambda(\mu') d\mu'. \qquad (9)$$

Note that our definition of G_λ differs from that of Stenflo (1982, 2005) only by a negative sign. This sign change is made to account for the circumstance that the positive Q direction in the theoretical calculations of scattering matrices is defined to be perpendicular to the limb, while it is defined to be parallel to the limb in the observations. In Stenflo (2005), this sign change has been made in the final expression for G_λ presented in that paper (see his Equation (31)). For convenience of our purposes, it is sufficiently accurate to assume that the actual limb darkening $(I_\lambda(\mu)/I_\lambda(\mu = 1))$ can be represented by a parabolic type function $f_\lambda(\mu)$ as given by Equation (7). This allows us to perform the integration in Equation (9) analytically. $f_\lambda(\mu)$ is defined for the outward hemisphere (positive μ) only. For the inward hemisphere (negative μ) it is assumed to be zero, which is a valid assumption at the surface ($\tau_\lambda = 0$). Thus, we obtain

$$k_{G,\lambda}(\mu) = \left(\frac{3a_{0,\lambda}}{64} + \frac{a_{1,\lambda}}{20} \right)$$
$$\times \frac{(1 - \mu^2)}{1 - a_{0,\lambda} - a_{1,\lambda} + a_{0,\lambda} \, \mu + a_{1,\lambda} \, \mu^2}. \qquad (10)$$

Note that the determination of $a_{0,\lambda}$ and $a_{1,\lambda}$ and thus of $k_{G,\lambda}(\mu)$ crucially depends on the observed CLV of Stokes I. Hence, we made a dedicated set of observations on 2009 January 10 to record the intensity spectrum with great precision at several μ positions. The slit was oriented parallel to the geographic north pole and placed at different μ positions. Since the intensity flat field of the detector in the spectrograph focus is very important for this type of observation, we applied a careful flat-fielding procedure by combining images taken while the telescope was moving in a random pattern around disk center and the spectrograph grating position was unchanged, with images taken while the grating rotated to smear the spectrum. The μ positions were calculated to a high degree of accuracy using three methods, namely (1) the slit position calculated from the digitized slit jaw image, (2) the slit position calculated from the guiding system (primary image guider; Küveler et al. 1998), and (3) the slit position calculated with the aid of the encoder system, giving the telescope position in right ascension and declination. The various $I_\lambda(\mu)$ recordings were brought to a common wavelength scale through interpolation, so that the wavelength positions of all the blend lines perfectly match for the different $I_\lambda(\mu)$ observations. Otherwise, due to small wavelength drifts between the different $I_\lambda(\mu)$ recordings, one can get spurious peaks in $k_{G,\lambda}(\mu)$ due to gradient effects in the vicinity of the blend lines.

Figure 3 shows a plot of the geometric depolarization factor $k_{G,\lambda}(\mu)$ for $\mu = 0.1$. It can also be called "anisotropy factor" as it is largely governed by G_λ (see Equation (9)). The resemblance of $k_{G,\lambda}(\mu)$ to the $I_\lambda(\mu)$ spectra is very striking in the far wings. However, it also has a distinctive shape in the core and wings of the Ca ı 4227 Å line. The anisotropy factor has a minimum in both the core of the main line and the cores of the surrounding blend lines. It is largest in the line wings, where
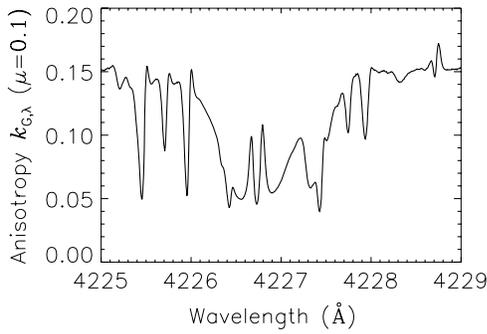
Figure 3. Plot of the geometric depolarization or anisotropy factor $k_{G,\lambda}(\mu)$ as a function of λ for disk position $\mu = 0.1$.

it reaches a nearly constant value. We note that our anisotropy plot resembles the anisotropy curve J_0^2/J_0^0 shown as the solid line in Figure 5 (right bottom panel) of Holzreuter et al. (2005) for the same line.

3.3. Atomic and Atmospheric Data

Ca I 4227 Å is a resonance line for which the lower level is the ground state, and the coupling to other bound states of Ca I may be neglected (see Faurobert-Scholl 1992). Therefore, a 2-level model atom is a reasonably good approximation. The $(^1S_0 \rightarrow \ ^1P_1 \rightarrow \ ^1S_0)$ scattering transition produces a triplet line in the presence of strong magnetic fields. In weak fields the partially split m states coherently superpose (interfere) to give rise to the Hanle effect. We take the required atomic data for this line from Faurobert-Scholl (1992). The radiative width is $\Gamma_R = 2.18 \times 10^8 \ s^{-1}$. The Doppler width is given by

$$\Delta\lambda_D = \frac{\lambda_0}{c}\sqrt{\frac{2kT}{M_a} + v_{turb}^2} \qquad (11)$$

where c is the speed of light, k is the Boltzmann constant, and M_a is the mass of a Ca I atom. For a temperature $T = 6000$ K and a turbulent velocity $v_{turb} = 2 \ km \ s^{-1}$, the Doppler width is 35.9 mÅ. The corresponding damping parameter $a_R = \Gamma_R/(4\pi\Delta\nu_D) = 2.8 \times 10^{-3}$.

3.4. Model for the Nonmagnetic Scattering Polarization

It is well known that strong resonance lines like Ca I 4227 Å can be modeled only when PRD effects are taken into account. Therefore, we need to use appropriate PRD matrices in our LSA approach. The relevant expressions can either be taken from Domke & Hubeny (1988), or computed from our Hanle–Zeeman theory with $B = 0$ (see Sampoorna et al. 2007a, 2007b). Further, we now need to generalize Equation (1), which was formulated for frequency coherent scattering in the laboratory frame by Stenflo (1982). The expression for the line contribution to the linear polarization Q/I is given by

$$P_{Q,line} = \frac{\int R_{21}(\lambda, \lambda', \Theta) \, k_{G,\lambda'}(\mu) \, I_{\lambda'}(\mu = 1) \, d\lambda'}{\int R_{11}(\lambda, \lambda', \Theta) \, I_{\lambda'}(\mu = 1) \, d\lambda'}. \qquad (12)$$

Here, $R_{i1}(\lambda, \lambda', \Theta)$ are the redistribution matrix elements for $i = 1, 2$. They depend on the scattering angle

$$\Theta = \cos^{-1}[\cos\theta\cos\theta' + \sin\theta\sin\theta'\cos(\phi - \phi')], \qquad (13)$$

where (θ, ϕ) and (θ', ϕ') are respectively the outgoing and incoming ray directions with respect to the atmospheric normal.

The expression for $P_{Q,line}$ (i.e., Equation (12)) can be justified as follows. According to LSA the emergent polarization is produced by the last scattering event. The incident radiation is unpolarized, so we only need to consider the single-scattering redistribution matrix elements $R_{i1}(\lambda, \lambda', \Theta)$ as done in Equation (12). The angular integration over incoming angles is avoided by applying the $k_{G,\lambda'}(\mu)$ factor, which embodies the effect of the anisotropy of the incident radiation field. Thus, the matrix element R_{21} simply needs to be scaled with this factor and integrated over all incoming wavelengths. Conceptually, we have here decomposed the angular integral into two parts. The first part consists of a unidirectional delta function scaled with $k_{G,\lambda'}(\mu)$. The second part is isotropic and vanishes on angular integration with R_{21}. Only the delta function contributes to the polarization.

When CRD is assumed, we have $R_{i1}(\lambda, \lambda', \Theta) = H(\Delta\lambda', a)H(\Delta\lambda, a)P_{i1}(\Theta)$ where $H(\Delta\lambda, a)$ is the Voigt function (see below) and $P_{i1}(\Theta)$ are the nonmagnetic Rayleigh phase matrix elements (see, e.g., Stenflo 1994 for their expressions). Thus, under CRD Equation (12) becomes wavelength independent and therefore is valid only in the line core (see Section 4.1.2).

For the calculations presented in this paper, we choose $\cos\theta = \mu = 0.1$, for which the observations were made. For the scattering geometry we use $\cos\theta' = 1$ and $\phi = \phi' = 0$. The collisional depolarization factor k_c is self-consistently contained in R_{21} and R_{11} through proper branching ratios. We use the AD PRD matrices for all our modeling purposes, unless stated otherwise.

In order to model the observations we also need to take into account the contributions of the continuum, namely the continuum opacity and the continuum polarization. They are included in our model as follows :

$$\frac{Q}{I} = S\left[P_{Q,line}\frac{H(\Delta\lambda, a)}{H(\Delta\lambda, a) + C} + P_c\frac{C}{H(\Delta\lambda, a) + C}\right]. \qquad (14)$$

$H(\Delta\lambda, a)$ is the Voigt function that describes the absorption probability for the Ca I 4227 Å line, with damping parameter a given by

$$a = \frac{\Gamma_R + \Gamma_I + \Gamma_E}{4\pi\Delta\nu_D} = a_R\left[1 + \frac{\Gamma_I + \Gamma_E}{\Gamma_R}\right]. \qquad (15)$$

Since the inelastic collision rate $\Gamma_I \ll \Gamma_E$, we set $\Gamma_I = 0$. For a given choice of Γ_E/Γ_R, the free parameters of our model are S, C, P_c. The global scaling parameter S is adjusted such that the amplitude of the modeled Q/I blue wing maximum agrees with the observed value. Ideally S should be close to unity. Large departures from unity may be due to transfer effects and/or collisional depolarization. The continuum opacity parameter C plays the dominant role. It allows us to reproduce the overall shape of the observed Q/I in the near and far wings of the Ca I 4227 Å line. In particular, it determines the wavelength positions where the maximum wing polarization is reached, beyond which the polarization starts to decline again. The continuum polarization P_c only determines the asymptotic shape of Q/I in the very far wings and does not play an important role here. P_c is fixed by the asymptotic behavior of Q/I far from the line center. From the atlas of Gandorfer (2002) we determine the ratio $r_{obs} = (P_c)_{obs}/P_{wing,max(4227)}$. In our modeling, we always choose P_c such that $r_{model} = r_{obs}$. The fitting procedure is as follows.

   1. Choose a given value of C.

2. Choose a P_c that makes $r_{\text{model}} = r_{\text{obs}}$.
3. Find a value of S that makes $(Q/I)_{\text{wing,max}}$ of the model agree with the observed value.

Iterate (1) to (3) until the best fit is obtained. The fitting procedure is repeated for different choices of Γ_E/Γ_R, so that we obtain S, C, and P_c as functions of Γ_E/Γ_R.

3.5. Model for Magnetic Scattering Polarization

Assuming that the nonmagnetic anisotropy factor $k_{G,\lambda}(\mu)$ is still valid in the presence of weak fields, we extend the model of Section 3.4 to include the Hanle effect. We further assume that the same $k_{G,\lambda}(\mu)$ can be used for both Q/I and U/I. This implies that the decomposition of the angular integral into a contribution from a unidirectional delta function scaled with $k_{G,\lambda}(\mu)$, while the rest represents isotropic scattering, is equally valid for both Q/I and U/I. This is a reasonably good approximation, but we plan to test it in future work. Thus, the model U/I profile for the Hanle effect is given by

$$\frac{U}{I} = S P_{U,\text{line}} \frac{H(\Delta\lambda, a)}{H(\Delta\lambda, a) + C} , \qquad (16)$$

where

$$P_{U,\text{line}} = \frac{\int R_{31}(\lambda, \lambda', \Theta) k_{G,\lambda'}(\mu) I_{\lambda'}(\mu = 1) d\lambda'}{\int R_{11}(\lambda, \lambda', \Theta) I_{\lambda'}(\mu = 1) d\lambda'}. \qquad (17)$$

Q/I is given by Equations (14) and (12), but now R_{21} and R_{11} contain magnetic field contributions. For the scattering redistribution matrix elements R_{i1} with $i = 1, 2, 3$ we use the Hanle–Zeeman theory (see Sampoorna et al. 2007a, 2007b), although we may also use approximation II of Bommier (1997). Note that in a plane-parallel atmosphere the continuum polarization contribution to the U/I is zero. However, as shown by Trujillo Bueno & Shchukina (2009), in a real three-dimensional model atmosphere this contribution to U/I is actually a nonzero quantity whose local value fluctuates in sign at the spatial scales of the horizontal inhomogeneities that produce symmetry breaking in the radiation field. The fitting procedure for the weak magnetic field case is as follows.

1. First the model parameters S, C, P_c for different choices of Γ_E/Γ_R are fixed by fitting the Q/I observed in a quiet region (see Section 3.4).
2. For these fixed parameters we use the magnetic redistribution matrix to compute U/I and Q/I for various choices of Γ_E/Γ_R and the vector magnetic field $\boldsymbol{B}$ parameters.
3. We then explore which combinations of $\boldsymbol{B}$ and Γ_E/Γ_R best reproduce the observations.

4. RESULTS AND DISCUSSION

4.1. Model Fit of the Nonmagnetic Q/I

Using the procedure described in Section 3.4, we fit the observed nonmagnetic Q/I data shown as the solid line in the top panel of Figure 2. We recall that such a fit fixes the values of the free parameters S, C, and P_c.

4.1.1. Role of the Geometric Depolarization Factor $k_{G,\lambda}(\mu)$

To illustrate the important role of the anisotropy factor $k_{G,\lambda}(\mu)$ we present in Figure 4 the model profiles computed using $k_{G,\lambda}(\mu)$ determined from observations (solid line) and computed with a flat $k_{G,\lambda}(\mu)$ (dashed line). For the flat $k_{G,\lambda}(\mu)$ we choose
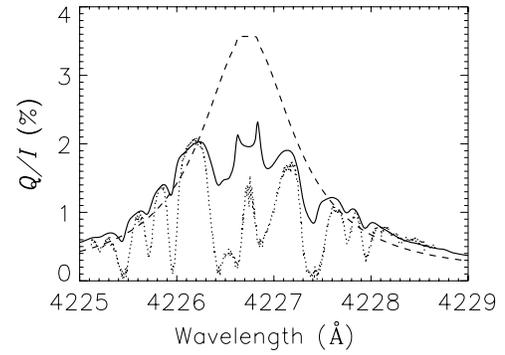

Figure 4. Role of $k_{G,\lambda}(\mu)$. The solid line is the model profile computed using pure $R_{\text{II-AD}}$ type redistribution and $k_{G,\lambda}(\mu)$ determined from observations. The dotted line is the observed Q/I in the nonmagnetic region (same as the solid line in the top panel of Figure 2). The dashed line is the model profile computed using pure $R_{\text{II-AD}}$ type redistribution but with a flat $k_{G,\lambda}(\mu) = 0.112$ for all wavelengths. The free parameters obtained from the model fit are $S = 0.325$, $C = 9.7 \times 10^{-5}$, and $P_c = 0.25\%$.

the value of nonflat $k_{G,\lambda}(\mu)$ at the wavelength of the Q/I blue wing peak, and keep it constant for all other wavelengths. To compute the model profiles in Figure 4 (solid and dashed lines) we have used the collisionless PRD matrix (i.e., AD pure $R_{\text{II-AD}}$ type redistribution). The free parameters obtained by the model fit are $S = 0.325$, $C = 9.7 \times 10^{-5}$, and $P_c = 0.25\%$.

Clearly the entire structuring of the Q/I model profile, with the minima around the Ca I 4227 Å Doppler core and the blend line depressions, are all related to the $k_{G,\lambda}(\mu)$ structure (see Figure 3). The blend line minima of the model profile (solid line) are less deep than in the observed spectrum (dotted line). The main reason why the computed blend lines are not sufficiently deep in Q/I is not due to $k_{G,\lambda}(\mu)$ alone, but because we have disregarded that the blend line opacities can have intrinsic polarizability $W_2 = 0$ and thus dilute the Ca I 4227 Å line photons with unpolarized photons. We have chosen to ignore this property here, to avoid introducing more free parameters and keep the model as simple as possible.

4.1.2. The Role of Partial Frequency Redistribution

The use of frequency coherent scattering in the laboratory frame (static atoms) is physically incorrect due to Doppler redistribution. It can still be used as a good approximation in the line wings, but becomes invalid in the line core. For a correct treatment we need PRD.

In Figure 5, we compare model profiles computed with different redistribution mechanisms. The coherent scattering (CS) limit can, for example, be obtained from the general PRD expression by choosing $R = R_{\text{CS}} = H(\Delta\lambda, a) \delta(\lambda - \lambda')$ as the redistribution function. The angular dependence of the scattering process is then given by the nonmagnetic Rayleigh phase matrix. One can see in Figure 5 that except in the line core, where CS differs greatly from the AD PRD (heavy solid line, which is the same as the solid line in Figure 4), pure coherent scattering (CS, dashed line) provides a good approximation at the Ca I 4227 Å wing frequencies. In fact, coherent scattering gives deeper minima in the blend lines than PRD. This is because when $C = 0$ and $P_c = 0$, the model profile obtained with coherent scattering exactly mimics the $k_{G,\lambda}(\mu)$ spectrum, while PRD modifies it significantly in the inner core of the Ca I 4227 Å line and also in the cores of the blend lines (because although $R_{\text{II-AD}}$ has coherent peaks in the wings, such peaks
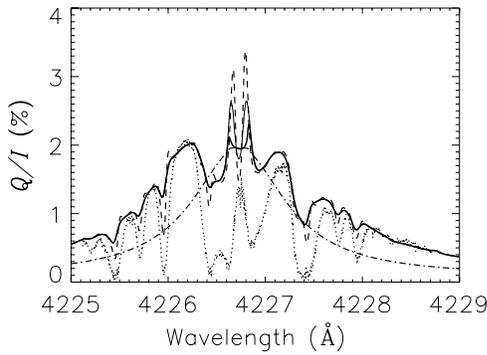
Figure 5. Role of PRD. The heavy solid and dotted lines are the same as in Figure 4. The dashed line is the model profile computed with frequency coherent scattering (CS), while the dot-dashed line is computed assuming CRD. The thin solid line is the model profile with $R_{\text{II-AA}}$, while the heavy solid line has been computed with $R_{\text{II-AD}}$.

are not exactly delta functions unlike the case of pure coherent scattering and cause some broadening).

Figure 5 also shows a model profile computed with the assumption of CRD (dot-dashed line). We recover the CRD limit from the general expression by using $R = R_{\text{CRD}} = H(\Delta\lambda', a)H(\Delta\lambda, a)$ for the redistribution function. The shape of the model profile obtained with CRD can be easily understood from Equations (14) and (12). In CRD, the redistribution matrix elements are $R_{21} = 0.7425\,R_{\text{CRD}}$, and $R_{11} = 1.2425\,R_{\text{CRD}}$ (see, e.g., Nagendra 2003 for the Rayleigh phase matrix expression). Thus, $P_{Q,\text{line}}$ becomes wavelength independent and is given by

$$P_{Q,\text{line}} = 0.6\,\frac{\int H(\Delta\lambda', a)\,k_{\text{G},\lambda'}(\mu)\,I_{\lambda'}(\mu = 1)\,d\lambda'}{\int H(\Delta\lambda', a)\,I_{\lambda'}(\mu = 1)\,d\lambda'}. \quad (18)$$

Therefore, the line contribution becomes constant at a value that is found to be 6%. The shape of the CRD model profile is then entirely due to the factor $H(\Delta\lambda, a)/(H(\Delta\lambda, a) + C)$ in Equation (14). As $C \ll 1$, this factor is close to unity at line center, where we have $(Q/I)_{\Delta\lambda=0} \approx 6\% \times S$. For the value of $S = 0.325$ derived from the best fit (obtained with PRD), $(Q/I)_{\Delta\lambda=0} \approx 2\%$. As we move away from the line center, the factor $H(\Delta\lambda, a)/(H(\Delta\lambda, a) + C)$ decreases monotonically, and there is no possibility of modeling the observed Q/I maxima of the Ca I 4227 Å line anywhere in the line wings. We emphasize that it is not only the anisotropy of the incident radiation field that governs the shape and magnitude of the wing maxima in Q/I, but also a realistic redistribution mechanism, namely, PRD.

We also show in Figure 5 a comparison between the model Q/I profile based on the AA $R_{\text{II-AA}}$ (thin solid line) and AD $R_{\text{II-AD}}$ (heavy solid line) PRD mechanisms. Both succeed well in modeling the wing peaks within our LSA framework. The differences are noticeable only in the line core. The double peak in the line core has also been seen in the radiative transfer modeling by Holzreuter et al. (2005), who use $R_{\text{II-AA}}$. Note that the same qualitative features of $(Q/I)_{\text{line-core}}$ that we have found here for different line scattering mechanisms (CS, CRD, $R_{\text{II-AA}}$, and $R_{\text{II-AD}}$) may not be reproduced with the same details in full-scale radiative transfer modeling.

Comparison with the observed Q/I spectrum shows that LSA allows us to model the Q/I wings extremely well. With LSA we can fit the envelope (above the blend line depressions) of the observed Q/I. The line core of Ca I 4227 Å is, however, not modeled so well by LSA, although correct qualitative features like the Q/I dips around the Doppler core are reproduced. This is also the case after including the contribution from $R_{\text{III-AD}}$

type scattering through the introduction of elastic collisions (see below). This means that LSA does not work well enough in the line core, and that one may need radiative transfer physics to explain the core shape of Q/I. This question is something we should like to pursue in a future work by modeling the Ca I 4227 Å line with full radiative transfer, to allow us to clarify and identify what aspect of radiative transfer is the source of the difference that we see in the line core.

The fit of the observations with the last scattering model leads to a scaling factor S of 32.5% rather than unity, which may be due to collisional depolarization, although radiative transfer effects may also cause deviations from LSA. If the main contribution to the scaling parameter S comes from elastic collisions, then the scaling parameter gives us an estimate of the elastic collision rate Γ_{E}. In the following section, we discuss the effect of Γ_{E} on the model profiles, as it plays an important role in the modeling.

4.1.3. Role of Elastic Collisions Γ_E

In the previous sections we considered only limiting cases of frequency redistribution, namely frequency coherent scattering in the atomic frame (i.e., pure $R_{\text{II-AD}}$ in the laboratory frame) and CRD. We now consider more realistic situations, where both types of scattering may occur, i.e., a weighted combination of $R_{\text{II-AD}}$ and $R_{\text{III-AD}}$ type scattering. The weights are the branching ratios given by

$$A = \frac{\Gamma_{\text{R}}}{\Gamma_{\text{R}} + \Gamma_{\text{I}} + \Gamma_{\text{E}}}, \quad (19)$$

for coherent scattering (in the atomic frame—$R_{\text{II-AD}}$ type), and

$$B^{(K)} = \frac{\Gamma_{\text{E}} - D^{(K)}}{\Gamma_{\text{R}} + \Gamma_{\text{I}} + \Gamma_{\text{E}}}\,\frac{\Gamma_{\text{R}}}{\Gamma_{\text{R}} + \Gamma_{\text{I}} + D^{(K)}}, \quad (20)$$

which represents the fraction of the scattering processes for which the atom is subject to elastic collisions that destroy the frequency coherence, but not the $2K$-multipole atomic polarization. Here, $D^{(K)}$ is the rate of destruction of the $2K$-multipole, with $K = 0, 1, 2$ (note that $D^{(0)} = 0$). As we are only considering linear polarization, only $D^{(2)}$ is relevant. $D^{(2)}$ is related to Γ_{E} through $D^{(2)} = \text{constant} \times \Gamma_{\text{E}}$. The classical value of this constant is 0.5 (see Stenflo 1994). Using an accurate form for the interatomic potential, Faurobert-Scholl et al. (1995; see also Faurobert-Scholl 1996) estimate this constant to be 0.6 for the Ca I 4227 Å line. In our modeling, we therefore use $D^{(2)} = 0.6\Gamma_{\text{E}}$.

For the Ca I 4227 Å line Γ_{E} is due to collisions with neutral hydrogen (see Auer et al. 1980; Faurobert-Scholl 1992). The effect of Γ_{E} on Q/I is to reduce the polarization at all wavelengths, and thereby make the scaling parameter S become unity. Thus, an increase in the elastic collision rate Γ_{E} causes a depolarization throughout the line profile. The effect of $D^{(2)}$ is limited to the line core, where it is somewhat similar to that of Γ_{E}, but it does not affect the line wings, in contrast to Γ_{E}.

With Γ_{E} as a free parameter, we have determined by model fitting the parameters S, C, P_c for different choices of Γ_{E}. The combinations of free parameters thus determined are listed in Table 1. We note that as $\Gamma_{\text{E}}/\Gamma_{\text{R}}$ increases, the continuum opacity parameter C increases as well, and the scaling parameter S approaches unity. The continuum polarization P_c remains nearly constant. Furthermore, introduction of elastic collisions improves the fit to the observed Q/I spectrum, in particular around the red wing maximum, and also the computed blend line minima become deeper as compared with the pure $R_{\text{II-AD}}$ model fit (compare the solid lines in Figures 4 and 6). For

Table 1
The Free Parameters S, C, P_c Determined from the Model Fit for Different
Choices of Γ_E/Γ_R

Γ_E/Γ_R	S	C	P_c (%)
0	0.325	9.7E-5	0.25
0.5	0.345	1.5E-4	0.25
1	0.38	2.2E-4	0.25
2	0.43	3.5E-4	0.25
3	0.485	5.0E-4	0.25
5	0.67	1.0E-3	0.23
10	1.00	2.1E-3	0.13

Figure 6. Model fit obtained for $\Gamma_E/\Gamma_R = 10$ (solid line). The dotted line is the observed Q/I. Note how well the observed Q/I wings are fitted by the computed model profile.

illustration we present in Figure 6 an example of a model fit obtained for $\Gamma_E/\Gamma_R = 10$.

4.2. An Attempt to Model the (Q/I,U/I) Wing Signatures

Next, we try to model the U/I observation shown in Figure 2 with the modeling procedure described in Section 3.5. Observations show wing maxima in the $-U/I$ spectrum around 4226.2 Å and 4227.2 Å, which correspond approximately to ± 15 Doppler widths from the 4226.74 Å line center. Note that the observed U/I spectrum happens to be negative in our present recordings. In general, U/I spectra of either sign are equally likely, as they are due to a rotation angle that can be both positive and negative. In this paper, we refer to the "$-U/I$ spectrum" to avoid confusion when we speak about polarization maxima in the line wings. Ambiguity might arise if we would instead speak of wing minima in U/I, since the absolute value of the polarization always has wing *maxima* in both the $+U/I$ and $-U/I$ cases.

The parameters required for the modeling are Hanle $\Gamma_B = geB/(2m\Gamma_R)$ in standard notation, and (ϑ_B, φ_B) representing the orientation of a directed magnetic field, defined with respect to the vertical direction in the atmosphere. The elastic collision rate Γ_E is also used as a free parameter. We recall that the parameters S, C, and P_c determined from the nonmagnetic model fit for a given choice of Γ_E/Γ_R (as listed in Table 1) are kept constant when the magnetic field parameters are varied. In this way, we have attempted to model the observed $(Q/I, U/I)$ spectra outside the so-called "nonmagnetic" regions, and at the spatial locations where the $(Q/I, U/I)$ wing signatures are seen.

4.2.1. Wing Peaks of Q/I

The framework that has been developed in the previous sections for modeling the nonmagnetic Q/I can still be used in the magnetized case with the modifications described in Section 3.5. For the purpose of discussion we introduce a quantity $\Delta(Q/I) = (Q/I)_{mag} - (Q/I)_{nonmag}$, which is a measure of the depolarization caused by the combined effect of magnetic and collisional depolarization that we get in PRD. In the top panel of Figure 2, we observe depolarization in Q/I (with respect to the nonmagnetic Q/I), not only in the line core but also in the wings (compare the solid and dashed lines in that figure). To model these observations (the dashed line in Figure 2), we varied the field parameters $(\Gamma_B, \vartheta_B, \varphi_B)$ and the elastic collision strength Γ_E/Γ_R. Our study shows that with the choice of pure R_{II-AD} to represent the PRD mechanism we do not get any wing depolarization ($\Delta(Q/I) \approx 0$), regardless of the choice of the field parameters. However, when we introduce elastic collisions we find that for an optimum choice of the combination $(\Gamma_B, \Gamma_E/\Gamma_R)$, we do get wing depolarization ($\Delta(Q/I) \neq 0$) in Q/I. Let us next discuss briefly a few
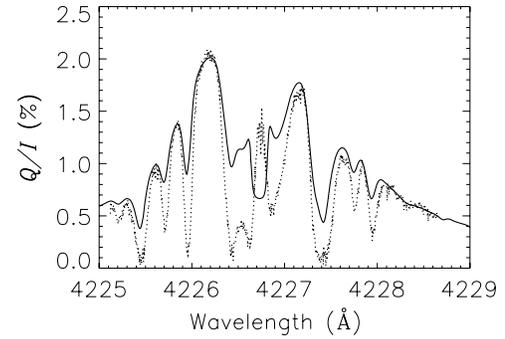
interesting aspects of this study. All the tests have been made for the field strength range $0.3 \leqslant \Gamma_B \leqslant 10$.

In the line core $\Delta(Q/I)$ decreases toward zero as Γ_E/Γ_R increases. This shows that for large values of Γ_E/Γ_R the effect of collisional depolarization dominates over the effect of magnetic depolarization in the line core. In the line wings $\Delta(Q/I) \approx 0$ when $\Gamma_B < 3$. For $3 \leqslant \Gamma_B \leqslant 10$ the wing signature $\Delta(Q/I)$ initially increases slowly with Γ_E/Γ_R, and then decreases toward zero with a further increase of the collision strength. For example, when $(\Gamma_B, \Gamma_E/\Gamma_R) = (10, 10)$ we observe Hanle depolarization that extends into the wings as shown in Figure 7 (compare the heavy solid and the thin solid lines), but no wing peaks are obtained in $\Delta(Q/I)$ as represented by the dashed line. If we further increase Γ_E/Γ_R (say to 100), then $\Delta(Q/I)$ vanishes in the line wings and becomes almost zero also in the line core, implying that the collisional depolarization effect again dominates over the magnetic depolarization effect. These two competing effects together decide the extent of depolarization in the wings.

4.2.2. Wing Peaks of U/I

Our modeling efforts turn out to be unsuccessful in reproducing the observed wing maxima in $-U/I$, contrary to our expectations. We expected that the elastic collisions play a significant role in transferring the Hanle effect from the line core to the line wings without destroying the atomic polarization (Nagendra et al. 2003; Bianda et al. 2003; Sampoorna et al. 2007b). This expectation is satisfied to some extent for Q/I for an optimum choice of the parameter pair $(\Gamma_B, \Gamma_E/\Gamma_R)$, but even in this optimized case we fail to reproduce the wing maxima that are observed in $\Delta(Q/I)$. In the case of U/I we find that for $\Gamma_B < 3$ the amplitude of U/I in the line core gradually decreases when Γ_E/Γ_R increases, but correspondingly no wing peaks appear at all. For $3 \leqslant \Gamma_B \leqslant 10$, U/I in the line core initially increases slightly with Γ_E/Γ_R but then decreases with the further increase in the collision strength. Again no wing peaks appear. Variations of the magnetic field parameters also do not help to reproduce the U/I wing peaks (like they failed to reproduce the $\Delta(Q/I)$ wing peaks). The line core peak in U/I, on the other hand, sensitively responds to variations of all the above free parameters in a manner that is well understood (Nagendra et al. 2002).

5. CONCLUSIONS

In the present paper, we have developed a simple framework based on the LSA to model the Second Solar Spectrum. This
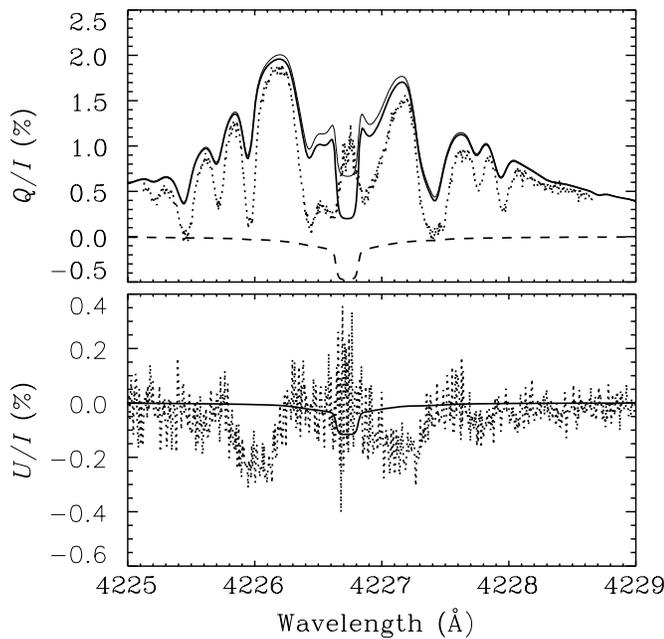
Figure 7. Attempt to model the $(Q/I, U/I)$ wing signatures. The observations (dotted lines) shown here correspond to the "magnetic observations" presented in Figure 2. In the Q/I panel the heavy solid line represents the magnetic model profile, the thin solid line the nonmagnetic model profile, and the dashed line their difference. In the U/I panel, the solid line represents the magnetic model profile. The parameters used are $(\Gamma_B, \vartheta_B, \varphi_B; \Gamma_E/\Gamma_R) = (10, 90°, 135°; 10)$.

approximation gives excellent fits to the linear polarization that is observed in the wings of spectral lines, as demonstrated for the case of the Ca I 4227 Å line. However, fitting the line core polarization may require the solution of the polarized radiative transfer equations (including PRD), at least for strong resonance lines. The most important quantity in our modeling is the anisotropy factor $k_{G,\lambda}(\mu)$, which we determine from the observed center-to-limb variation of the Stokes I spectrum. The detailed wavelength variation of the limb darkening function plays a fundamental role and is responsible in particular for the occurrence of Q/I minima that surround the core region and separate it from the wing maxima. Another key ingredient is the appropriate PRD matrix to be used. The detailed validity range of the LSA (extent of its applicability in the line cores of strong lines and throughout the line profiles in the case of weak lines) needs to be explored by benchmark tests with full-scale radiative transfer before the diagnostic potential of this approach can be fully exploited.

We have applied the LSA framework to explore the question whether the observed spatial variations in the Q/I and U/I wings of the Ca I 4227 Å line may be explained in terms of the Hanle effect, which usually is confined to the Doppler core of spectral lines but could in principle become active in the far line wings through frequency redistribution mediated by elastic collisions. Such Hanle-like wing signatures were noticed for the first time in active regions by Bianda et al. (2003), but in the present paper we report observations showing that these wing signatures are present in quiet solar regions as well. Our attempts to model these $(Q/I, U/I)$ wing signatures failed to reproduce them. Both the $\Delta(Q/I)$ profile of the Q/I spatial variations and the $-U/I$ profile are observed to have maxima in the wings, similar in shape to the Q/I nonmagnetic profile. However, the $\Delta(Q/I)$ and $-U/I$ modeling failed to retrieve this property, although we searched the whole parameter space of collision rates and magnetic field parameters.

This null result appears to rule out a direct magnetic field origin (via the Hanle effect) of the observed spatial variations of the scattering polarization in the line wings, in contradiction to earlier suggestions (Nagendra et al. 2003; Bianda et al. 2003; Sampoorna et al. 2007b), at least within the framework of the currently available PRD theory. This points in the direction of a nonmagnetic interpretation, which may include local deviations from a plane-parallel stratification (see Manso Sainz & Trujillo Bueno (1999), for some information on the possible effects) with an inhomogeneous solar atmosphere containing "hot spots" (see Holzreuter & Stenflo (2007), who used this mechanism to interpret the Q/I and U/I fluctuations seen abundantly in the Ca K line). The local density inhomogeneities may also cause significant fluctuations of the collisional depolarization rate. Detailed analysis of these possibilities is outside the scope of the present paper, but such alternative interpretations clearly need to be explored. Ideally, one would like to do two-dimensional mapping of the Stokes vector (rather than work with single slit positions) with high spatial resolution to map the polarization signatures together with the intensity structures to examine whether the nonmagnetic interpretation is viable.

The nonmagnetic interpretation is not without its own problems. Thus, with a simple-minded model for spatially varying deviations from a plane-parallel stratification one would expect a spatial correlation between the line wing fluctuations seen in Q/I and U/I, but such a correlation seems to be weak or nearly absent in our observations. This indicates that the three-dimensional atmospheric structuring that one would need is more complex, and that we may have to consider a mixture of geometry and collisional effects. It is important to quantify how much the atmosphere deviates from a plane-parallel stratification in lines of various strengths, and how these deviations are spatially structured, and coupled to the opacity structure within the line as we move from the core to the wings of the line. While this is a challenging problem, it is within reach with the new generation of observing facilities that are becoming available. The problem can also be approached by numerical simulations to generate three-dimensional atmospheric models, and then use three-dimensional radiative transfer to compute the linearly polarized line profiles that emerge from this atmosphere (e.g., as done by Trujillo Bueno et al. 2004; Trujillo Bueno & Shchukina 2007 for the Sr I 4607 Å line assuming CRD). Such a project for the Ca I 4227 Å line for which PRD effects are important would be extremely demanding on computing resources, but it is something that also will soon be within reach.

REFERENCES

Auer, L. H., Rees, D. E., & Stenflo, J. O. 1980, A&A, 88, 302
Belluzzi, L., Trujillo Bueno, J., & Landi Degl'Innocenti, E. 2007, ApJ, 666, 588
Bianda, M., Solanki, S. K., & Stenflo, J. O. 1998a, A&A, 331, 760
Bianda, M., Stenflo, J. O., Gandorfer, A., & Gisler, D. 2003, in ASP Conf. Ser. 286, Current Theoretical Models and Future High Resolution Solar Observations: Preparing for ATST, ed. A. A. Pevtsov & H. Uitenbroek (San Francisco, CA: ASP), 61
Bianda, M., Stenflo, J. O., & Solanki, S. K. 1998b, A&A, 337, 565
Bianda, M., Stenflo, J. O., & Solanki, S. K. 1999, A&A, 350, 1060
Bommier, V. 1997, A&A, 328, 726
Domke, H., & Hubeny, I. 1988, ApJ, 334, 527

Faurobert, M., & Arnaud, J. 2002, A&A, 382, L17
Faurobert, M., Derouich, M., Bommier, V., & Arnaud, J. 2009, A&A, 493, 201
Faurobert-Scholl, M. 1992, A&A, 258, 521
Faurobert-Scholl, M. 1996, Sol. Phys., 164, 79
Faurobert-Scholl, M., Feautrier, N., Machefert, F., Petrovay, K., & Spielfiedel, A. 1995, A&A, 298, 289
Fluri, D. M., & Stenflo, J. O. 2001, in ASP Conf. Ser. 236, Advanced Solar Polarimetry—Theory, Observation, and Instrumentation, ed. M. Sigwarth (San Francisco, CA: ASP), 205
Frisch, H., Anusha, L. S., Sampoorna, M., & Nagendra, K. N. 2009, A&A, in press
Gandorfer, A. 2000, The Second Solar Spectrum, Vol. I , 4625 Å to 6995 Å line (Zurich: VdF), ISBN No. 3 7281 2764 7
Gandorfer, A. 2002, The Second Solar Spectrum, Vol II, 3910 Å to 4630 Å line (Zurich: VdF), ISBN No. 3 7281 2844 4
Gandorfer, A. 2005, The Second Solar Spectrum, Vol III, 3160 Å to 3915 Å line (Zurich: VdF), ISBN No. 3 7281 3018 4
Gandorfer, A. M., et al. 2004, A&A, 422, 703
Holzreuter, R., Fluri, D. M., & Stenflo, J. O. 2005, A&A, 434, 713
Holzreuter, R., Fluri, D. M., & Stenflo, J. O. 2006, A&A, 449, L41
Holzreuter, R., & Stenflo, J. O. 2007, A&A, 472, 919
Küveler, G., Wiehr, E., & Bianda, M. 2003, Astron. Nachr., 324, 308
Küveler, G., Wiehr, E., Thomas, D., Harzer, M., Bianda, M., Sütterlin, P., Epple, A., & Weisshaar, E. 1998, Sol. Phys., 182, 247
Landi Degl'Innocenti, E., & Landolfi, M. 2004, Polarization in Spectral Lines (Dordrecht: Kluwer)
Manso Sainz, R., & Trujillo Bueno, J. 1999, in Solar Polarization, ed. K. N. Nagendra & J. O. Stenflo (Boston: Kluwer), 143

Nagendra, K. N. 2003, in ASP Conf. Ser. 288, Stellar Atmosphere Modeling, ed. I. Hubeny, D. Mihalas, & K. Werner (San Francisco, CA: ASP), 583
Nagendra, K. N., Frisch, H., & Faurobert, M. 2002, A&A, 395, 305
Nagendra, K. N., Frisch, H., & Fluri, D. M. 2003, in ASP Conf. Ser. 307, Solar Polarization, ed. J. Trujillo Bueno & J. Sanchez Almeida (San Francisco, CA: ASP), 227
Omont, A., Smith, E. W., & Cooper, J. 1973, ApJ, 182, 283
Pierce, K. 2000, in Allen's Astrophysical Quantities, ed. A. N. Cox (4th ed.; New York: Springer), 355
Ramelli, R., Bianda, M., Trujillo Bueno, J., Merenda, L., & Stenflo, J. O. 2005, in ESA SP-596, Chromospheric and Coronal Magnetic Fields, ed. D. E. Innes, A. Lagg, & S. K. Solanki (Katlenburg-Lindau: Published on CDROM), 82.1
Sampoorna, M., Nagendra, K. N., & Stenflo, J. O. 2007a, ApJ, 663, 625
Sampoorna, M., Nagendra, K. N., & Stenflo, J. O. 2007b, ApJ, 670, 1485
Sampoorna, M., Nagendra, K. N., & Stenflo, J. O. 2009, in ASP Conf. Ser. 405, Solar Polarization 5, ed. S. V. Berdyugina, K. N. Nagendra, & R. Ramelli (San Francisco, CA: ASP), 93, in press
Stenflo, J. O. 1980, A&A, 84, 68
Stenflo, J. O. 1982, Sol. Phys., 80, 209
Stenflo, J. O. 1994, Solar Magnetic Fields (Dordrecht: Kluwer)
Stenflo, J. O. 2004a, Rev. Mod. Astron., 17, 269
Stenflo, J. O. 2004b, Nature, 430, 304
Stenflo, J. O. 2005, A&A, 429, 713
Trujillo Bueno, J. 2009, in ASP Conf. Ser. 405, Solar Polarization 5, ed. S. V. Berdyugina, K. N. Nagendra, & R. Ramelli (San Francisco, CA: ASP), 65, in press
Trujillo Bueno, J., & Shchukina, N. 2007, ApJ, 664, L135
Trujillo Bueno, J., & Shchukina, N. 2009, ApJ, 694, 1364
Trujillo Bueno, J., Shchukina, N., & Asensio Ramos, A. 2004, Nature, 430, 326